X-ray absorption by a microgranular sample

Janis Timoshenko,[1,*] David Kordus,[1] Jette K. Mathiesen,[1,†] Uta Hejral,[1] Patrik Zeller,[2] Gereon Behrendt,[2] Eylül Öztuna,[2] Jihao Wang,[2] Zahra Gheisari,[2] Rene Eckert,[3] Stephan Reitmeier,[3] Andreas Reitzmann,[3] Holger Ruland,[4] Jan Folke,[4] Thomas Lunkenbein,[2] and Beatriz Roldan Cuenya[1]

[1]*Fritz-Haber Institute of Max Planck Society, Interface Science Department, Faradayweg 4-6, 14195 Berlin, Germany*

[2]*Fritz-Haber Institute of Max Planck Society, Department of Inorganic Chemistry, Faradayweg 4-6, 14195 Berlin, Germany*

[3]*Clariant Produkte (Deutschland) GmbH, 83052 Heufeld, Germany*

[4]*Max Planck Institute for Chemical Energy Conversion, Department Heterogeneous Reactions, Stiftstraße 34-36, 45470, Mülheim an der Ruhr, Germany*

(Received 7 March 2025; accepted 13 June 2025; published 10 July 2025)

Sample homogeneity on the microscopic scale is critical for the reliable interpretation of x-ray absorption spectra collected in transmission mode. Unfortunately, it is not always easy to ensure it in practice. Especially in *operando* studies of catalysts and functional materials, the microstructure of the sample can evolve during its operation and even become the key descriptor for understanding structure-property relationships of the material, as exemplified by the transformations taking place in technical iron-based catalysts for ammonia synthesis under operating conditions. Here we present a simple approach for the identification and quantification of the material's microgranular structure effect on its x-ray absorption spectrum. We demonstrate that the quantitative information on the sizes of microscopic sample particles can be extracted from the observed distortions in the x-ray absorption near-edge structure spectra. The obtained insight can also be used to correct for the artifacts in extended x-ray absorption fine structure fitting, associated with the presence of microscopic inhomogeneities in the sample.

DOI: 10.1103/bqg7-kb24

I. INTRODUCTION

X-ray absorption spectroscopy (XAS) is a premier method for probing the local atomistic and electronic structures in a broad range of functional materials, including heterogeneous catalysts under working conditions [1–3]. In particular, x-ray absorption near-edge structure (XANES) spectroscopy provides the information about the chemical state and local symmetry of x-ray absorbing species, while extended x-ray absorption fine structure (EXAFS) spectroscopy probes the arrangements of neighboring atoms around the central absorbing atom. Conceptually, an x-ray absorption experiment is very simple, and requires just to measure the intensities of the x-rays before and after the sample (I_0 and I_T, respectively), while scanning the energy of the incident x-ray photons E. However, such XAS measurements in transmission mode require care with the sample preparation. In particular, the concentration of the x-ray absorbing species in the sample should be high enough to result in a significant attenuation of x-rays. At the same time, the sample should not be too concentrated, since at least some of the x-rays need to pass through the sample to result in a measurable I_T signal. The contribution of transmitted x-rays should also be much larger than the "leakage" signal due to the higher harmonics, radiation that is not attenuated by the sample, and other photons with the energies not matching the target energy of the incident monochromatic beam [4–7]. Furthermore, the distribution of x-ray absorbing species needs to be homogeneous in the entire x-ray irradiated area. Variations in sample thickness on the scale that is comparable to the x-ray penetration depth (a few microns for the x-rays with the energy of a few keV) will result in distortions of XANES and EXAFS features. While these requirements are well known [8–12], it is not always possible to satisfy them in practice. Important examples of such cases are the concentrated samples consisting of hard grains, e.g., metallic powders, that cannot be easily crushed to smaller particles [13]. Furthermore, the nonuniform microgranular structure of the sample can form and evolve *in situ*, e.g., during the reduction of the catalyst under pretreatment or under working conditions. The parameters characterizing the microstructure of the sample (e.g., the characteristic particle size) in this case can themselves be an important outcome of the experiment, and, thus cannot be dismissed just as a factor leading to the "artifacts" in spectra analysis. For XAS spectra collected in such cases it is thus important to recognize the distortions in spectral features associated with the nonuniform microstructure of the sample. Furthermore, it is highly desirable to develop a practical solution for quantifying these distortions, linking them to microstructure parameters. This is the main objective of this study. We particularly focus here on the analysis of powder samples, where the micrometer-sized grains of a concentrated sample are dispersed within

*Contact author: janis@fhi-berlin.mpg.de

†Present address: Technical University of Denmark, Department of Physics Fysikvej, Building 312, 2800 Kongens Lyngby, Denmark.

Published by the American Physical Society under the terms of the Creative Commons Attribution 4.0 International license. Further distribution of this work must maintain attribution to the author(s) and the published article's title, journal citation, and DOI. Open access publication funded by Max Planck Society.

the inert matrix. Such samples, prepared as pellets or as powders loaded into the capillaries, feature prominently in the XAS studies of concentrated materials, and, in particular, in *operando* investigations of powder catalysts.

We acknowledge here that the analysis of the effect of the sample thickness and inhomogeneities on XAS spectra has a very long history [10,13–19]. However, so far the majority of prior studies have focused predominantly on the analysis of the EXAFS part of the absorption spectra, while the effect of the sample inhomogeneity on the XANES features was largely neglected in the previous literature. For example, models for the analysis of the EXAFS amplitude reduction in simple cases featuring inhomogeneous samples containing regions with two [10,13] or three [14,15] different sample thicknesses have been developed. Lu and Stern, in turn, have modeled the effects of the particle size on EXAFS spectra of a single, close packed layer of large spherical particles [16]. Furthermore, more general models of EXAFS distortions featuring a continuous distribution of sample thicknesses have been discussed by Bunker [8] and Bausk *et al.* [17]. Nonetheless, although such studies are highly valuable, we argue here that such a focus on the EXAFS part of absorption spectra is not the best approach to address the questions that have arisen while investigating the heterogeneous granular material systems. Here we consider it essential to focus on the analysis of the previously mostly neglected distortions in the XANES features that we demonstrate provide a unique possibility to determine the microstructure parameters from XAS measurements. In this regard, one should mention that the numerical approaches for modeling the effects of sample inhomogeneity on XANES have been previously discussed by the excellent works of Scarrow [18] and Curis *et al.* [19]. Nonetheless, even though the analysis of the spectral distortions in these previous works was based on a similar model as the one discussed below, and the obtained spectra distortions qualitatively resemble our results, our analysis method presents some advantages. For practical applications it is important to not only be able to recognize such effects, but also to develop a robust method to quantify them, and account for them in data analysis, which is the main objective of the present study. We demonstrate here that the accounting for sample microstructure effects in XANES analysis can be done using a simple analytical fitting formula, which noticeably improves the reliability of the XANES spectra interpretation in heterogeneous samples. Importantly, our approach also enables the quantification of the microstructure parameters from XANES data. We also show that the effect of granular sample structure on EXAFS spectra, in turn, can largely be reduced to a decrease in the EXAFS amplitude, which agrees with prior findings [10,13–15]. EXAFS analysis, however, does not provide a clear path for the analysis of the microstructure of the sample. Indeed, we show that the considered effect is indistinguishable from many other sample- and instrumentation-related effects that all could result in diminished EXAFS amplitudes.

As an example of a system with inevitably large particle sizes, we consider here an industrially applied iron-based catalyst for ammonia production. This technologically important system has been interrogated by means of x-ray absorption spectroscopy for decades, with the majority of existing studies reporting on curious deviation of the XAS spectra for the working catalyst from that of bcc-type iron reference [20,21]. In some instances this effect was hypothesized to be linked to the nanostructure of the sample (presence of undercoordinated Fe sites) [20], but Niemann *et al.* had already hinted that it could also be a result of sample inhomogeneities [21]. In this study, we address this issue and confirm that the previously observed distortions of Fe *K*-edge XAS spectra for an industrial ammonia catalyst are related to the microstructure rather than nanostructure of the sample. More importantly, we also demonstrate the usefulness of XAS for quantitative characterization of the microstructure of this key catalytic material. As highlighted in our recent work, the mesoscopic multiscale structure of a technical ammonia catalyst formed under working conditions plays the key role in catalytic performance of this material [22].

II. METHODS

A. X-ray absorption measurements

All XAS measurements were performed at the P64 beamline at the PETRA III synchrotron. A Si(111) double channel monochromator was used for energy selection. Measurements were carried out in transmission mode using ionization chambers filled with 1024 mbar of N_2 as detectors. Beam size is $0.5 \times 0.5\,\mathrm{mm}^2$.

We compare here the spectra collected *ex situ* for spent iron catalyst powder after several days under reaction, and the spectra collected *operando*. For *ex situ* measurements, the sample powder was mixed with boron nitride and pressed into a 13 mm pellet. Sample preparation has been carried out in a glovebox to avoid exposure of the reduced sample to air. The prepared pellet was sealed with Kapton tape and taken out of the glovebox immediately before the XAS data acquisition. For *ex situ* measurements, we prepared two different samples. The first sample was used without any additional treatment of the powder. For the second sample, before preparing the pellet, we sieved the sample powder with the finest sieve available (opening size 20 μm), to remove at least the largest powder particles.

For the *operando* measurements, the iron oxide powder sample was loaded into our in-house-built *operando* cell, featuring a 1 mm (outer diameter) quartz capillary (Hilgenberg GmbH). The inner diameter of the capillary was 0.9 mm. It was connected to a gas dosing system and a mass spectrometer for product detection. The sample powder (multipromoted iron oxide) was crushed in the mortar, sieved, and carefully mixed with boron nitride in a ca. 1:8 ratio, and loaded into the capillary. The dilution of the sample is necessary to achieve reasonable intensity of transmitted x-rays. The sample was gradually heated to 500 °C in a reaction mixture (1:3 N_2:H_2 at 14 bars). Pressure was regulated using a manual back-pressure regulator, while the heating was ensured by an electric heater located below the capillary. The temperature was controlled by using a EuroTherm temperature controller, with a thin thermocouple inserted inside the capillary to track the temperature. Afterwards, the sample was cooled down to room temperature to collect high quality EXAFS data.

Processing of XAS data is carried out using a set of in-house-built *Wolfram Mathematica* scripts. Extraction of the

EXAFS spectra is carried out using the LARCH code [23]. Fitting of the EXAFS spectra is carried out using the FEFFIT code [24]. Fitting is carried out in R space in the R range between 1.2 and 2.9 Å. The k range used for Fourier transformation is between 3 and 12 $Å^{-1}$. The fitting model consists of the contribution of two coordination shells, which in the ideal bulk bcc Fe structure have coordination numbers 8 and 6, respectively, with interatomic distances ca. 2.482 and 2.866 Å, respectively. For EXAFS data fitting we employ the so-called isotropic contraction and expansion model, commonly used to fit spectra for bcc structures [25]. It is assumed here that the changes in the interatomic distances R with respect to a reference structure can be described as $R_{eq}(1+\varepsilon)$, where R_{eq} is the respective bond length in the reference structure, and ε is the expansion coefficient, which is a fitting variable that is identical for all coordination shells considered. During the fitting we thus refine the coordination number N_{Fe1} and expansion coefficient ε. The coordination number for the second coordination shell is set to $N_{Fe2} = N_{Fe1}\frac{6}{8}$. The interatomic distances for the first two coordination shells, R_{Fe1} and R_{Fe2}, respectively, are then set to $(1+\varepsilon)$ 2.482 Å and $(1+\varepsilon)$ 2.866 Å [25]. Disorder factors for both coordination shells are fitted independently. We also refine the correction to the photoelectron reference energy ΔE_0. The amplitude reduction factor $S_0^2 = 0.72$ is obtained from the fit of EXAFS spectrum for the Fe foil.

B. X-ray total scattering measurements

Ex situ x-ray total scattering (TS) experiments for the spent Fe catalyst were carried out at 76.69 keV (0.1617 Å) at beamline XPDF I15-1, Diamond Light Source, UK. The undiluted catalyst sample was packed in a polyimide capillary (from Cole-Palmer) with an outside diameter of 1.05 mm and a wall thickness of 0.025 mm. An empty polyimide capillary was measured to ensure a correctly defined background for the background subtraction. TS data were collected at ambient conditions in transmission geometry using a PerkinElmer detector XRD 4343 CT (432 × 432 mm^2 active area, 150 × 150 μm^2 pixel size). The sample-to-detector distance and instrumental broadening parameters ($Q_{broad} = 0.014$ $Å^{-1}$ and $Q_{damp} = 0.013$ $Å^{-1}$) were calibrated using a Si NIST standard. Automated processing in the DAWN software package was used for azimuthal integration, masking, and normalization of the data [26].

The x-ray TS data were Fourier transformed with XPDFSUITE to obtain the pair distribution functions (PDFs) using $Q_{instru} = 23.0$ $Å^{-1}$, $Q_{min} = 0.5$ $Å^{-1}$, and a Q_{max} of 23.0 $Å^{-1}$ [27]. The background correction was performed by subtracting the scattering signal obtained from an empty polyimide capillary. Modeling of the experimental PDF was done using PDFGUI in the r range from 1.5 to 60 Å, in which a least-squares optimization procedure was performed between a theoretical PDF of the bcc Fe structure and the experimental PDF [28,29]. The refined parameters included the unit cell parameters, the δ_2 parameter describing local correlated atomic movement, the scale factor, a spherical particle diameter, and the isotropic atomic displacement parameters (ADPs) for the Fe atoms in the structure.

C. Scanning electron microscopy

For scanning electron microscopy (SEM) measurements, a prereduced technical ammonia catalyst was placed inside a flow reactor compatible with SEM imaging, featuring a quartz tube reactor inside the chamber of a commercially available environmental SEM (ESEM, FEI 200 Quanta FEG). The catalyst was heated by an infrared laser (808 nm, maximum 110 W) [30]. A metallic stainless-steel mesh supported the catalyst aliquot inside the tube, and a spot-welded K-type thermocouple was used for temperature control. Pure gases (Westfalen 5.0) were dosed into the quartz tube reactor by mass-flow controllers (Bronckhorst), with the corresponding flow rates 3.0 ml N min^{-1} for H_2, 1.0 ml N min^{-1} for N_2, and 0.2 ml N min^{-1} for Ar. The gas lines were equipped with O_2/moisture filters (Agilent in-line purifier OT3-2). The catalyst was gradually heated to 500° C with a heating ramp rate of 12 K h^{-1}. At the end of the heating ramp, the catalyst was treated isothermally for an additional 225.2 h under continuous ESEM imaging. Images of the catalyst surface were acquired with the large field detector of the ESEM at acceleration voltages of 7.5–10 kV at a chamber pressure of 22 Pa and a pixel depth of 8 bits.

III. RESULTS AND DISCUSSION

A. Experimental characterization

Figure 1 compares Fe K-edge XANES and EXAFS spectra, collected *ex situ* (pellet) and *operando* (capillary) for a spent ammonia synthesis catalyst. For comparison, we also show a spectrum for steel powder (85.7% Fe, 13% Cr, 1% W, 0.3% Ti) from Ref. [31]. Steel powder in that work was similarly diluted with BN and pressed into a pellet. One can conclude that for all investigated samples the spectra correspond to a metallic iron state with bcc-like structure. However, while the positions of all XANES and EXAFS features match well those of the reference Fe foil, the amplitudes are very different. In particular, all postedge XANES and EXAFS oscillations are strongly suppressed, while the intensity of the prominent XANES shoulder feature in the preedge region (at ca. 7115 eV) is enhanced. The obtained spectra are also in good agreement with the findings of previous XAS studies on ammonia synthesis catalysts [20,21]. It is striking that the observed distortions of the spectra are qualitatively the same for pellets and for a sample in a capillary, and also for such different materials as ammonia synthesis catalysts and FeCr steel powder. The first indication that this effect can be related to powder particle sizes is that sieving the sample before preparation of the pellet clearly reduces the distortion, although it does not allow us to get rid of it completely.

Interestingly, despite the distortions, conventional EXAFS fitting works well for all collected samples (Fig. 1(c) and Table I; EXAFS fitting results in k space for all samples are given in the Supplemental Material [32]; see Supplemental Fig. 1). The obtained values of the structure parameters look physically plausible, and the obtained fit R factor values are low. However, the Fe-Fe coordination numbers are low, and are inversely correlated with the degree of XANES distortions (the larger the distortions in the XANES region are, the lower the coordination numbers obtained from EXAFS analysis

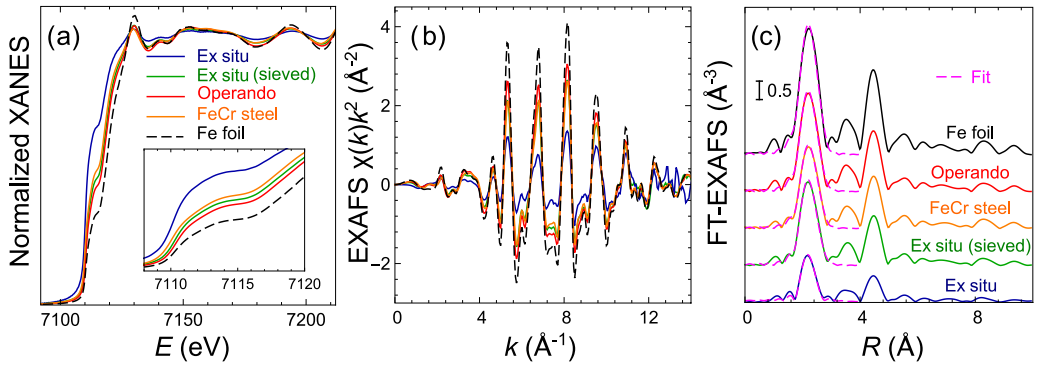


FIG. 1. Experimental Fe *K*-edge XAS data for metallic Fe powders. (a) Normalized Fe *K*-edge XANES spectra collected *ex situ* for pellets containing sieved and nonsieved spent industrial catalyst for ammonia synthesis, as well as *operando* data collected for the catalyst reduced in a reaction mixture in a quartz capillary. The spectrum for steel powder from Ref. [31], and the spectrum for the standard Fe reference foil are also shown. (b) Corresponding EXAFS spectra. (c) Moduli of Fourier transforms for the spectra shown in (b). Results of EXAFS fitting for the first two coordination shells in bcc iron structure are also shown with the dashed magenta line.

are). Furthermore, there is also an apparent correlation between the coordination numbers and the disorder factors (σ^2 factors) in the first coordination shell—the lower the coordination number values, the lower is the apparent disorder. The obtained values of interatomic distances in most cases match those obtained for Fe foil, although they seem to increase slightly upon an increase in spectra distortions, which might be related to the correlation between the interatomic distance values and the value for ΔE_0 (correction to photoelectron reference energy). The latter is found to increase with the distortion of the XAS spectra.

To independently confirm that the observed differences in the EXAFS spectra are not linked to the presence of undercoordinated Fe sites, we performed synchrotron-based x-ray total scattering measurements with subsequent pair distribution function (PDF) analysis (Fig. 2). PDF analysis provides information highly complementary to that of EXAFS, but relies on x-ray scattering rather than absorption. Similarly to EXAFS (and unlike conventional XRD), PDF analysis is well suited for investigations of small particles and other disordered phases with or without long-range order. However, unlike EXAFS, PDF analysis is also sensitive to medium-range order in the material. The presence of small crystallites (small coherent scattering domains) should be immediately evident as a disappearance of peaks at larger distances in the extracted PDF, in addition to changes in the peak intensities at lower distances. However, in our case the obtained PDF can be fitted very well with the bcc structure model of iron, and we do not observe any evidence of undercoordinated Fe sites or other unusual structural motifs (Supplemental Table S1 [32]). Indeed, the crystallite sizes obtained from the PDF fit (ca. 13.2 nm) should result in average first shell Fe-Fe coordination numbers and amplitudes of EXAFS spectra that are indistinguishable from the bulk values. Clearly, this is not what we observe in our EXAFS results (Table I, Fig. 1). This contradiction further supports the hypothesis that the observed

TABLE I. Fe *K*-edge EXAFS fitting results. Coordination number *N*, interatomic distance *R*, and disorder factors σ^2 for the first (Fe_1) and second (Fe_2) coordination shells in the bcc iron structure. Uncertainties of the last digit are given in parentheses. The values of the correction to the photoelectron reference energy ΔE_0 are also given, as well as the *R* factors characterizing the quality of the fit.

Sample		*N*	*R* (Å)	σ^2 (Å^2)	ΔE_0 (eV)	Fit *R* factor
Fe foil	Fe_1	8.0(3)	2.459(4)	0.0058(3)	–1.9(9)	0.9%
	Fe_2	6.0(2)	2.840(5)	0.0047(5)		
Operando	Fe_1	5.8(2)	2.461(3)	0.0051(2)	–1.4(6)	0.5%
	Fe_2	4.4(1)	2.842(3)	0.0048(4)		
FeCr	Fe_1	4.5(1)	2.467(3)	0.0047(2)	–1.2(5)	0.4%
steel	Fe_2	3.4(1)	2.849(3)	0.0042(3)		
Ex situ	Fe_1	4.5(1)	2.461(4)	0.0044(2)	–1.3(7)	0.6%
(sieved)	Fe_2	3.4(1)	2.842(4)	0.0047(5)		
Ex situ	Fe_1	1.6(2)	2.478(8)	0.0005(5)	2(2)	2.8%
	Fe_2	1.2(1)	2.859(9)	0.007(3)		

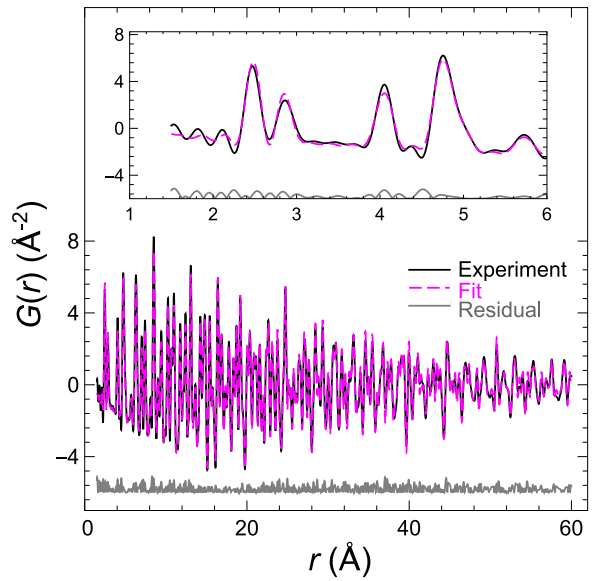


FIG. 2. Pair distribution function (PDF) extracted for the unsieved ammonia synthesis catalyst sample from the *ex situ* synchrotron-based PDF measurements. Fit to the bcc structure of metallic Fe is also shown with a dashed line. Inset shows the close-up of the contribution of the nearest coordination shells.

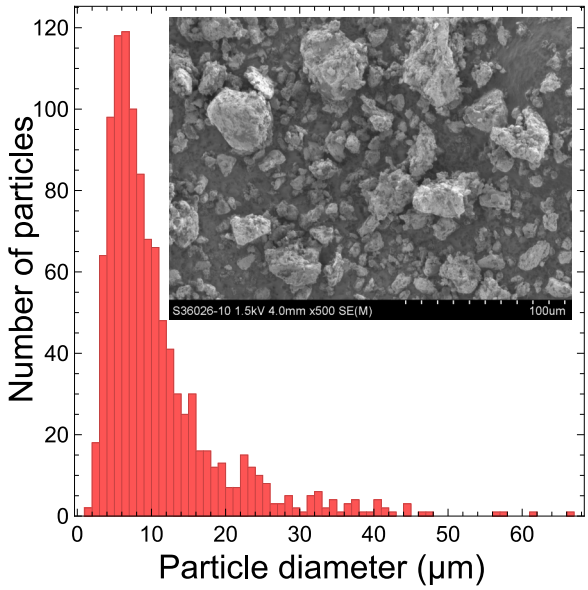


FIG. 3. SEM image of the spent unsieved ammonia synthesis catalyst, and the corresponding particle size distribution.

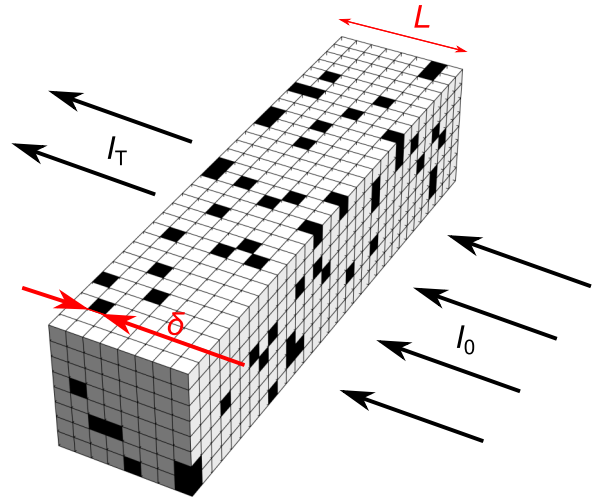


FIG. 4. Schematic depiction of x-ray absorption by a microgranular sample.

distortions in the XAS spectra are not related to changes in the local (nano-) structure of the material, but rather are attributed to differences in the material morphology on a microscopic level.

Indeed, the collected SEM data (Fig. 3) reveal that the investigated sample after reaction features large particles of a few micrometers in size. The particle size distribution peaks at the value of ca. 7 μm, with the average particle size being 11 μm (standard deviation: 8 μm). The presence of such large particles inevitably must have an effect on the XAS spectra, since a single particle of a size of 10 μm at the Fe *K*-edge already locally attenuates the x-ray flux about 30 times. The presence of such particles thus clearly needs to be accounted for in the quantitative analysis (both in EXAFS and XANES regions). Furthermore, since these particles are formed under the catalyst's working conditions, it is desirable to be able to extract the information on the size of these microparticles from XAS measurements. Indeed, in our recent work [22] we argue that the formation of such mesoscopic granular structure in a technical ammonia catalyst is driven by promoters present in the precatalytic material. It is a key feature of this catalytic system responsible for its activity; thus the ability to track the evolution of such granular structures is essential for understanding and rational optimization of this catalyst.

B. Effective absorption for a microgranular sample

The energy-dependent x-ray absorption $M(E)$ is defined according to the Beer-Lambert law as

$$M(E) = -\ln \frac{I_T}{I_0}. \tag{1}$$

For a homogeneous sample of uniform thickness d, the absorption is commonly described by a linear absorption coefficient $\mu(E) = M(E)/d$, which depends only on material properties. The latter expression, however, cannot be used directly to describe the absorption by a nonuniform sample.

To account for the microstructure of the sample, we consider a simple discrete model featuring monodisperse grains with size δ, uniformly distributed within a matrix (Fig. 4). The grains can be porous, polycrystalline, or even consist of a mixture of different species. Thus the value of δ reflects the particle sizes as measured by microscopy, rather than the sizes of coherent scattering domains as probed by PDF or EXAFS. We further assume that the x-ray absorption by matrix is negligible. The sample area A is uniformly illuminated by the x-ray beam. The total sample thickness L is assumed to be uniform within the illuminated area, and thus this part of the diluted sample can be approximated with a parallelepiped. Importantly, in our model L is much larger than δ. We note that for the powder samples within a thin capillary the cylindrical shape of the capillary can also be considered. However, as recently demonstrated by Wang *et al.*, the effect of capillary curvature on the shape of XAS features, as well as the effect of an inhomogeneous beam profile, can be neglected, as long as the size of the beam is smaller than the diameter of the capillary [33].

In such a model, each x-ray beam can pass through a portion of the sample containing zero, one, or several powder particles. The total x-ray absorption for this particular x-ray beam thus will be $\exp[-\mu(E)\nu\delta]$, where $\nu \in [0, \nu_{\max}]$ is the number of encountered powder particles, with $\nu_{\max} = \frac{L}{\delta}$. The probability for the x-ray beam to encounter k particles can be described by the binomial distribution $P(\nu) = C_\nu^{\nu_{\max}} p^\nu (1-p)^{\nu_{\max}-\nu}$, where p is the probability for each voxel in our discretized model to be occupied by a powder particle. It is directly linked to the dilution of the powder in the matrix, $p = V/V_0$, where V is the volume occupied by the powder particles and V_0 is the total volume of the sample (including powder particles and matrix).

The average attenuation of an x-ray beam then can be calculated as $\sum_{\nu=0}^{\nu_{\max}} P(\nu)\exp[-\mu(E)\nu\delta]$, and the x-ray flux after the sample thus will be $\tilde{I}_T = I_0 \sum_{\nu=0}^{\nu_{\max}} P(\nu)\exp[-\mu(E)\nu\delta]$. This summation, in fact, can be carried out analytically,

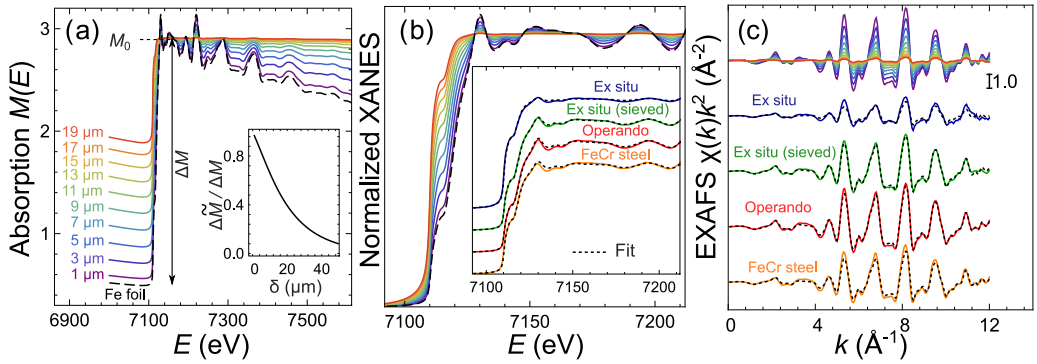


FIG. 5. Modeling particle size effect on Fe *K*-edge XAS data for bcc iron. (a) True absorption $M(E)$ for an Fe foil and apparent absorption $\tilde{M}(E)$ calculated using Eq. (4) for different particle grain sizes δ as indicated in the plot. Inset shows the ratio between apparent and true absorption jumps for different δ values. (b) Normalized Fe *K*-edge XANES spectra extracted from the data shown in (a). Inset in (b) shows the best fits to experimental XANES data for metallic iron powder samples using Eq. (8). Spectra in the inset are shifted vertically for clarity. (c) k^2-weighted EXAFS spectra $\chi(k)k^2$ extracted from the data shown in (a), as well as the comparison between experimental EXAFS spectra for metallic iron powder samples and the EXAFS spectra extracted from the calculated $\tilde{M}(E)$ using δ values as obtained from XANES fitting. EXAFS spectra are shifted vertically for clarity. The same color coding is used in (a–c).

resulting in a relatively simple expression:

$$\tilde{I}_T = I_0[p(e^{-\delta\mu(E)} - 1) + 1]^{\nu_{\max}}. \tag{2}$$

The effective absorption can now be calculated as

$$\tilde{M}(E) = -\ln\frac{\tilde{I}_T}{I_0} = -\nu_{\max}\ \ln[p(e^{-\delta\mu(E)} - 1) + 1]. \tag{3}$$

Importantly, in most practical cases involving particles of concentrated sample, the volume of the matrix significantly exceeds the volume of the powder particles, resulting in $p \ll 1$. In this case Eq. (3) can be further simplified as

$$\tilde{M}\ (E) \approx \tilde{M}_0(1 - e^{-\delta\mu(E)}). \tag{4}$$

The $\tilde{M}_0 = pL/\delta$ term here cancels out during the conventional normalization of XANES or EXAFS data. This is highly useful, since it can be difficult to assess and control the value of catalyst dilution p in practice: it depends on the density of the matrix and that of the material powder, but also on the sample packing density, which inevitably will vary from one sample to another.

As a result, the shape of the XAS spectrum, defined by the $1 - e^{-\delta\mu(E)}$ term, does not depend on the dilution of the powder, but only on the particle size δ and the intrinsic absorption coefficient of the material $\mu(E)$. This allows us to use Eq. (4) to actually extract information on powder particle grain sizes by simply fitting the measured XAS spectra (*vide infra*). We also note that Eq. (4) suggests that for samples with very small grain size $[\delta\mu(E) \ll 1]$, the effect of particle grain size on the spectral shape becomes negligible, as expected: indeed, $1 - e^{-\delta\mu(E)}$ in this case can be approximated with $\delta\mu(E)$, and δ in this term cancels with the δ term in the $\tilde{M}_0$.

As an example, Fig. 5(a) shows the evolution of the absorption spectra (before normalization), calculated for a metallic bcc-type Fe sample with varied particle grain size, using the experimental spectrum for $d = 9$ μm Fe foil to derive $\mu(E)$. $\tilde{M}_0$ for each curve here is set to $\mu_0 d/(1 - e^{-\delta\ \mu_0})$, where μ_0 is the linear absorption coefficient for Fe foil above the edge (at $E_1 = 7162$ eV). This convention ensures that the total apparent absorption for all cases remains the same and equal to that of Fe foil, and mimics the process of sample thickness optimization in experimental measurements.

As one can see, for the fixed total absorption of the sample, the increase in the powder particle grain size results in a decreased absorption edge jump $\Delta\tilde{M}(E)$. With particle sizes becoming larger than a few tens of microns, the edge jump becomes essentially 0 [inset in Fig. 5(a)]. The unexpectedly low edge step for a sample with a high total absorption thus could be a first indication that the microstructure of the sample will distort the spectral features. Indeed, in addition to the decrease of the absorption edge, the increased particle grain sizes decrease the amplitude of the postedge oscillations and reduce the overall slope of the $M(E)$ function after the absorption edge, but also increase the relative amplitude of the preedge features. The latter is best seen when one uses the conventional procedure to extract from the XAS data the normalized XANES spectra [Fig. 5(b)]. One immediately can see the striking resemblance between the distortions of XANES spectra, as predicted by our model, with the ones we observed in experimental data in Fig. 1.

C. XANES for a microgranular sample

While Eq. (4) provides the possibility to calculate the changes in the total absorption spectra due to the presence of micrograins knowing the true absorption spectrum $M(E)$, in practice to evaluate this effect in experimental XANES data $X(E)$ it is more convenient to calculate the apparent $\tilde{X}(E)$ XANES spectrum from the true XANES spectrum. In particular, in the common case when the material is not phase pure, but rather a mixture of different species, the true XANES spectrum can be calculated just as a sum of XANES spectra for individual components, weighted by their concentrations, while the true total absorption $M(E)$ depends also on the densities of all components, which are nontrivial to assess experimentally.

We first note that the true XANES $X(E)$ is obtained from the total absorption $M(E) = \mu(E)d$ by subtracting the smooth background function $M_B(E)$, which includes the preedge

TABLE II. Particle sizes in the units of inverse linear absorption jumps (D) and in micrometers (δ) obtained from fitting experimental XANES data in Fig. 1 using Eq. (8).

Sample	D	δ (μm)	Fit R factor
Operando	0.90 ± 0.01	3.19 ± 0.04	0.014%
FeCr steel	1.49 ± 0.01	5.31 ± 0.04	0.016%
Ex situ	2.94 ± 0.01	10.46 ± 0.05	0.009%
Ex situ (sieved)	1.198 ± 0.006	4.27 ± 0.02	0.004%

background and the slope of the postedge background, and normalizing the resulting spectrum by edge step ΔM, where the latter can be expressed as a difference between $M(E)$ and $M_B(E)$ at some energy point E_1 slightly above the absorption edge:

$$X(E) = \frac{M(E) - M_B(E)}{M(E_1) - M_B(E_1)}. \tag{5}$$

By analogy, the apparent XANES spectrum can be calculated from the apparent total absorption $\tilde{M}(E)$ and apparent background $\tilde{M}_B(E)$:

$$\tilde{X}(E) = \frac{\tilde{M}(E) - \tilde{M}_B(E)}{\tilde{M}(E_1) - \tilde{M}_B(E_1)}. \tag{6}$$

Using Eq. (4) to link the total and apparent absorption and inserting it into Eq. (6), we obtain

$$\begin{aligned}\tilde{X}(E) &= \frac{\exp\left[-M_B(E)\delta/d\right] - \exp\left[-M(E)\delta/d\right]}{\exp\left[-M_B(E_1)\delta/d\right] - \exp\left[-M(E_1)\delta/d\right]} \\ &= S(E)\frac{1 - \exp\left(-[M(E) - M_B(E)\delta/d]\right)}{1 - \exp\left(-[M(E_1) - M_B(E_1)\delta/d]\right)} \\ &\approx \frac{1 - \exp\left(-[M(E) - M_B(E)]\delta/d\right)}{1 - \exp\left(-[M(E_1) - M_B(E_1)]\delta/d\right)},\end{aligned} \tag{7}$$

where we used the fact that for smoothly changing backgrounds in the vicinity of the absorption edge the term $S(E) = e^{\frac{M_B(E_1) - M_B(E)}{d/\delta}}$ can be, to a good accuracy, approximated with 1.

It is easy to see from Eq. (5) that the expression in the exponent in the numerator of Eq. (7) is just proportional to the true XANES $X(E)$, while the expression in the exponent in the denominator is proportional to the true absorption jump $\Delta\mu$:

$$\tilde{X}(E) = \frac{1 - \exp\left[-D\,X(E)\right]}{1 - \exp\left[-D\right]}, \tag{8}$$

where $D = \delta\Delta\mu$ is the particle size expressed in the units of inverse linear absorption jumps for a given material. Equation (8) is a convenient fitting formula that can be used to include the effect of the microstructure in XANES modeling, and to compare the particle sizes in different samples. If $\Delta\mu$ is known, it allows one also to directly estimate the particle sizes in micrometers.

In the inset of Fig. 5(b), we use Eq. (8) to find the best fit to experimental XANES data shown in Fig. 1. In all cases, as $X(E)$ we use the XANES spectrum for Fe foil, and we use least-squares fitting to obtain the best value for D, reported in Table II. As one can see, in all cases Eq. (8) provides excellent agreement with experimental observations, confirming that the observed distortions in the XANES features can be fully explained by the microstructure of the sample. We then use the $\Delta\mu$ value for metallic Fe (0.281 μm^{-1} as calculated from the $\Delta M = 2.53$ edge jump at the Fe K edge for 9 μm thick Fe foil) to calculate effective particle sizes δ. We also observe that the obtained effective particle sizes for the unsieved sample measured *ex situ* (ca. 10 μm) agree very well with the SEM results for this sample (the average particle size of ca. 11 μm). We note, however, that such an agreement should be considered with caution and not too overemphasized, due to the simplicity of our model (which considers monodisperse isotropic particles in contrast to the broad distribution of elongated particles visible in the SEM images), as well as due to the possible systematic errors in particle size determination by SEM, which might underestimate the contribution of the smallest particles (hardly visible on the background of larger particles), as well as that of the few largest particles, whose contribution varies strongly dependently on which image is selected for particle counting. Furthermore, the assumption that $\Delta\mu$ for the analyzed particles is the same as for the iron foil is also just an approximation. Indeed, $\Delta\mu$ is inversely proportional to material density, which for metallic particles formed under catalytic conditions can be very different from that of the reference bulk Fe foil, and will be strongly affected, e.g., by the porosity of the sample and the additional minority species (promoters) present in the technical catalyst. Nonetheless, the observed agreement between the particle sizes extracted by both methods suggests that our XAS-based approach provides meaningful estimates of the effective microscopic particle sizes.

More generally, the true $X(E)$ spectrum for the investigated material can differ from that of standard reference spectra also due to the actual differences in the local structure (e.g., strong structural distortions, or the presence of some unique structural motifs). The XANES part of the absorption spectra is usually less sensitive to these effects (in comparison to EXAFS). However, in some cases (e.g., in *in situ* experiments at very high temperatures, or in the presence of alloy formation) their influence cannot be ruled out completely. In these extreme cases, the extraction of the absolute values of microparticle sizes would be difficult. However, one can still get useful insight into relative differences in particle sizes, when comparing several spectra collected under similar conditions. In this case, one of the collected spectra can be used as an "internal standard," while the fitting variable D will provide information on the relative difference in the particle sizes for different measurements in the dataset. Indeed, in the range of D and $X(E)$ values of interest, Eq. (8) can be to a good accuracy (Fig. S2 [32]) approximated with

$$\tilde{X}(E) \approx \frac{1 - \exp\left[-\Delta\mathrm{D}\,X_0(E)\right]}{1 - \exp\left[-\Delta D\right]}, \tag{9}$$

where $\Delta D = D - D_0$ is the relative difference in particle sizes between the analyzed spectrum and the "internal reference" XANES spectrum $X_0(E)$. The latter is linked to the (unknown) true XANES spectrum through Eq. (8), with D set to D_0.

Finally, we emphasize that while in this work we focus on the XAS spectra for phase-pure materials, the nonlinear nature of Eq. (8) has particularly important implications for the analysis of samples with coexisting different species,

which is common for technical catalysts and other functional materials. Indeed, if the true XANES $X(E)$ is a weighted sum of different contributions $X(E) = \sum_i w_i X_i(E)$, where w_i is the concentration of the ith species, $\tilde{X}(E)$ is not equal to the $\sum_i w_i \tilde{X}_i(E)$, unless $D \ll 1$ (i.e., particle grains are very small). This means that the linear algebra based methods such as linear combination analysis (LCA) will not provide correct results, unless Eq. (8) is explicitly used to correct for particle size effect. We also highlight that in the case of microgranular mixture samples, we need to distinguish between situations where the sample consists of identical particles, with each particle being a mixture of different species (e.g., partially reduced), and the cases where the sample consists of a mixture of different particles (e.g., mixture of metallic and oxidized particles). LCA with the additional fitting parameter D as per Eq. (8) will provide correct results in the former case, but not in the latter.

D. EXAFS for a microgranular sample

From the total apparent absorption $\tilde{M}(E)$, using conventional approaches we can also extract EXAFS spectra $\tilde{\chi}(k)$. EXAFS spectra extracted from the model data in Fig. 5(a) are shown in Fig. 5(c), and exhibit the same trends as observed in the experimental EXAFS, the most obvious being the decrease in signal amplitude with the increased particle size δ. Indeed, if we simply overlap model EXAFS curves calculated for δ values as obtained from XANES analysis (Table II) with experimental data shown in Fig. 1, both sets of spectra agree nicely without additional modifications or fitting. This indicates that the δ values, as extracted from XANES, agree well also with the trends in the EXAFS spectra. It is, nonetheless, instructive to understand the origins of the distortions in the EXAFS spectra, and also how such distortions could affect the values of structure parameters extracted from EXAFS fitting. To the latter goal we first performed conventional EXAFS fitting of the model EXAFS curves in Fig. 5(c), without correcting for the particle size effect. The obtained results are summarized in Fig. 6, and strongly resemble our observations for the EXAFS spectra extracted from the experimental measurements. There is a full set of fitting results in the Supplemental Material (Fig. S2, Table S2 [32]). In particular, fit R factors in all cases are below 2%, indicating good fit quality. As expected, the increase in the powder particle size results in an apparent suppression of the Fe-Fe coordination number [Fig. 6(b)]. The effect of the particle size on Fe-Fe interatomic distance is less pronounced, and only for the larger particles we observe an apparent increase in Fe-Fe interatomic distance, which correlates with an increase in ΔE_0 value. Interestingly (and, again, in agreement with our observations from experimental data analysis), increase in particle size has a pronounced effect on disorder factor, with apparent σ^2 factor decreasing nearly linearly with the particle size, and even becoming negative for very large particles.

To understand these trends, we follow a similar approach as employed above for XANES modeling. First, we note that the EXAFS part of absorption spectra $\chi(E)$ is related to the total absorption as

$$\chi(E) = \frac{M(E) - M_{B,\,\mathrm{EXAFS}}(E)}{\Delta M}. \tag{10}$$

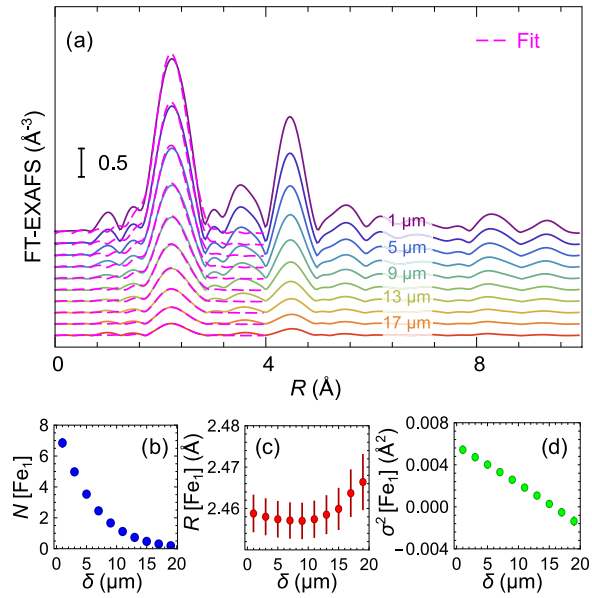


FIG. 6. Fitting EXAFS data extracted from apparent absorption for different particle sizes δ. (a) Moduli of Fourier transforms for the EXAFS spectra shown in Fig. 5(c), with δ values indicated in the plot, and the results of EXAFS fitting for the first two coordination shells in bcc structure. Spectra are shifted vertically for clarity. The obtained values of the first shell coordination number (b), average Fe-Fe distance (b), and corresponding disorder factor (c).

Equation (10) is similar to Eq. (5), but $\chi(E)$ is defined only in the postedge region, and the background function $M_{B,\,\mathrm{EXAFS}}(E)$ describes the smooth variations in the postedge background. Following the same route as above for XANES, the apparent EXAFS can be written as

$$\tilde{\chi}(E) = S_{\mathrm{EXAFS}}(E)\left(\frac{1 - \exp\left[-D\chi(E)\right]}{1 - \exp\left(-D\right)}\right). \tag{11}$$

Unlike it was for XANES, the energy-dependent changes in the background, as described by the term $S_{\mathrm{EXAFS}}(E) = e^{\frac{M_B(E_1) - M_{B,\mathrm{EXAFS}}(E)}{d/\delta}}$, cannot be neglected, and, in fact, are responsible for the decrease in the apparent disorder factor σ^2. To approximately account for these variations, we assume that the postedge background decreases linearly with energy [in agreement with the trend shown in Fig. 5(a)], allowing us to simplify $M_B(E_1) - M_{B,\mathrm{EXAFS}}(E) \approx -[\Delta M - |\frac{dM_{B,\mathrm{EXAFS}}}{dE}|(E - E_0)]$.

We then convert energies E to photoelectron wave numbers $k = \sqrt{\frac{2m_e}{\hbar^2}(E - E_0)}$, to obtain

$$\tilde{\chi}(k) \approx e^{2\sigma_0^2 k^2}\left(\frac{1 - \exp\left[-D\chi(k)\right]}{e^D - 1}\right), \tag{12}$$

with $\sigma_0^2 = \delta|\frac{dM_{B,\mathrm{EXAFS}}}{dE}|\frac{\hbar^2}{4m_e}$. Finally, we note that $\chi(k) \ll 1$, especially for larger k values (typically $k > 3$ Å^{-1}) that are commonly used for EXAFS fitting. This allows us to expand the exponent in the numerator, ending up with the approximate expression

$$\tilde{\chi}(k) \approx \frac{D}{e^D - 1}\chi(k)e^{2\sigma_0^2 k^2}. \tag{13}$$

From this expression it is obvious that the nonlinear decrease in the apparent coordination number is caused by the particle size dependent $\frac{D}{e^D-1}$ term, while the disorder factors σ^2 which dampen EXAFS amplitude at high k values as $e^{-2\sigma^2k^2}$ will be apparently decreased by σ_0^2, which is directly proportional to particle size δ. Overall, the key observation here is that the effect of the microgranular structure does not change the functional shape of the EXAFS equation. The effect of particle sizes is limited only to apparent changes in the values of parameters extracted from EXAFS fitting, and is thus practically indistinguishable from the effect of the true changes in the materials nanostructure. As a result, even in the presence of large microparticles EXAFS fitting will produce seemingly good results, with plausibly looking values for structure parameters. Ignoring the microparticle size effect in this case could lead to completely wrong conclusions about the actual structure of the material at hand.

IV. CONCLUSIONS

In this study we have investigated the effect of the presence of micrometer-sized particles on x-ray absorption spectra. We have demonstrated that this effect on XANES spectra can be reliably recognized and quantified, providing the possibility to use XAS to characterize not only the nanostructure, but also the microstructure of the sample. The obtained results are especially relevant for all XAS studies focusing on metallic powders, or any other powders with large hard grains that cannot be easily crushed or removed. We particularly highlight that such mesoscopic granular structures can also form during the *in situ* treatments or during the operation of the catalyst or functional material, as is the case in the industrial catalyst used for ammonia synthesis, and is thus an essential element of the structure-property relationship in the catalyst for this key technological process. Our approach allows now quantifying such changes, paving the road for understanding the activation mechanisms in technical ammonia catalysts and other high-loading metal-based heterogeneous catalytic systems, such as, for example, Fisher-Tropsch and other hydrogenation processes [34–36], where unsupported metal catalysts or heavily metal-loaded samples are employed. Furthermore, the applications of our method are not limited to catalysis only. Analysis of microparticulate metal structures via XAS is relevant also for studies of metallurgical processes [23,37] and additive manufacturing in general, and can find its applications also in environmental science [38,39], and geology and planetology [40,41]. Very recently, microscopic metallic iron powders have attracted attention also as a convenient, carbon-free energy storage material, calling for corresponding XAS investigations for further optimization of this exciting technology [42]. For all these applications, our method can provide highly useful insight. We furthermore highlight that XANES measurements for such concentrated samples as considered here do not necessarily require access to synchrotron radiation facilities, since such experiments (including *operando* and *in situ* studies) can now be successfully and conveniently carried out in laboratory-based XAS spectrometers [43–45]. Our approach can be equally well used for the interpretation of the data from such laboratory-based studies as for the synchrotron experiments.

At the same time, the obtained fitting formula [Eq. (8)] is very simple and easy to use, and is highly suited when modeling transmission XANES data for powder samples is undertaken. Indeed, the grain size parameter D in Eq. (8) is typically weakly correlated with the values of structural parameters (e.g., concentration values for different species in the linear combination model). Thus having this additional term in the fitting model results only in a slight increase of the fitting uncertainties. On the other hand, the consideration of powder particle grain sizes is expected to reduce the systematic errors in XANES fitting associated with the minor imperfections in the sample preparation, and could also immediately indicate possible issues with sample homogeneity.

We also highlight that the presence of microscopic grains has a strong effect on both the XANES and EXAFS regions of absorption spectra, but the reliable quantification of these effects is possible only from XANES analysis. In the EXAFS region the effect of sample macrostructure can be easily mistaken for the presence of undercoordinated sites and changes in the disorder. It is thus critical to always consider EXAFS data fitting together with the insight from XANES data, where the latter can allow to identify and correct for the particle size effect in EXAFS data interpretation.

ACKNOWLEDGMENTS

We would like to thank Prof. Robert Schlögl for support and fruitful discussions. The authors acknowledge the German Federal Ministry of Education and Research in the framework of the project Catlab (Project No. 03EW0015B). J.K.M. is grateful for funding from VILLUM FONDEN through Villum International Postdoc Grant No. VIL41388. We acknowledge DESY (Hamburg, Germany), a member of the Helmholtz Association HGF, for the provision of experimental facilities. Parts of this research were carried out at PETRA III and we would like to thank Dr. Wolfgang Caliebe for assistance in using beamline P64. Beamtime was allocated for Proposal No. I-20230325. The authors would like to also acknowledge the staff of beamline I15-1 at DIAMOND for experimental assistance during the x-ray total scattering experiments. This work was carried out with the support of Diamond Light Source, instrument I15-1 (Proposal No. CY28439-1).

DATA AVAILABILITY

The data that support the findings of this article are not publicly available because they contain commercially sensitive information. The data are available from the authors upon reasonable request.

[1] S. Bordiga, E. Groppo, G. Agostini, J. A. van Bokhoven, and C. Lamberti, Reactivity of surface species in heterogeneous catalysts probed by *in situ* x-ray absorption techniques, Chem. Rev. **113**, 1736 (2013).

[2] D. E. Sayers, E. A. Stern, and F. W. Lytle, New technique for investigating noncrystalline structures: Fourier analysis of the extended x-ray—absorption fine structure, Phys. Rev. Lett. **27**, 1204 (1971).

[3] J. J. Rehr and R. C. Albers, Theoretical approaches to x-ray absorption fine structure, Rev. Mod. Phys. **72**, 621 (2000).

[4] M. Rose and M. M. Shapiro, Statistical error in absorption experiments, Phys. Rev. **74**, 1853 (1948).

[5] E. A. Stern and K. Kim, Thickness effect on the extended-x-ray-absorption-fine-structure amplitude, Phys. Rev. B **23**, 3781 (1981).

[6] L. Parratt, C. Hempstead, and E. Jossem, "Thickness effect" in absorption spectra near absorption edges, Phys. Rev. **105**, 1228 (1957).

[7] S. M. Heald and E. A. Stern, Anisotropic x-ray absorption in layered compounds, Phys. Rev. B **16**, 5549 (1977).

[8] G. Bunker, *Introduction to XAFS: A Practical Guide to X-ray Absorption Fine Structure Spectroscopy* (Cambridge University Press, Cambridge, 2010), pp. 87–89.

[9] D. Gianolio, How to start an XAS experiment, in *X-Ray Absorption and X-Ray Emission Spectroscopy: Theory and Applications*, edited by J. A. van Bokhoven and C. Lamberti (Wiley, New York, 2016).

[10] S. Calvin, *XAFS for Everyone* (CRC Press, Boca Raton, FL, 2013), pp. 52–54.

[11] G. Meitzner, Experimental aspects of x-ray absorption spectroscopy, Catal. Today **39**, 281 (1998).

[12] S. Heald, in *EXAFS and Near Edge Structure: Proceedings of the International Conference, Frascati, Italy, September 13–17, 1982* (Springer, Berlin, 1983), p. 98.

[13] E. Voronina, D. Guy, and T. Miyanaga, Thickness effect correction in XAFS-spectroscopy: Temperature measurement approach, Nucl. Instrum. Methods Phys. Res., Sect. B **215**, 525 (2004).

[14] Y. A. Babanov, A. Ryazhkin, and T. Miyanaga, Correction of x-ray absorption spectra for thickness inhomogeneity and fluorescence of sample, Nucl. Instrum. Methods. Phys. Res. A **470**, 278 (2001).

[15] A. Ryazhkin, Y. Babanov, and T. Miyanaga, Thickness inhomogeneity and fluorescence effects in EXAFS spectroscopy for powder samples: Solution of the inverse problem, J. Synchrotron Radiat. **8**, 291 (2001).

[16] K.-Q. Lu and E. Stern, Size effect of powdered sample on EXAFS amplitude, Nucl. Instrum. Methods Phys. Res. **212**, 475 (1983).

[17] N. Bausk, S. Erenburg, and L. Mazalov, Correction of XAFS amplitude distortions caused by the thickness effect, J. Synchrotron Radiat. **6**, 268 (1999).

[18] R. Scarrow, Sample preparation for EXAFS spectroscopy, lecture notes for NSLS EXAFS course, 2002, https://docs.xrayabsorption.org/Workshops/NSLS2002/Scarrow.pdf.

[19] E. Curis, J. Osán, G. Falkenberg, S. Bénazeth, and S. Török, Simulating systematic errors in x-ray absorption spectroscopy experiments: Sample and beam effects, Spectrochim. Acta, Part B **60**, 841 (2005).

[20] G. Weinberg, B. Beran, M. Muhler, R. Schlögl, A. Dent, and T. Rayment, The micromorphology of the activated iron catalyst used for ammonia synthesis, Appl. Catal. A **163**, 83 (1997).

[21] W. Niemann, B. Clausen, and H. Topsøe, EXAFS studies of ammonia catalysts at synthesis conditions, Ber. Bunsengesellschaft Phys. Chem. **91**, 1292 (1987).

[22] K. Dembélé *et al.*, The Haber Bosch catalyst from solid state chemistry to mesotechnology, Adv. Energy Mater. 2500159 (2025).

[23] M. Newville, Larch: An analysis package for XAFS and related spectroscopies, J. Phys.: Conf. Ser. **430**, 012007 (2013).

[24] B. Ravel, and M. Newville, ARTEMIS ATHENA, HEPHAESTUS: Data analysis for x-ray absorption spectroscopy using IFEFFIT, J. Synchrotron Radiat. **12**, 537 (2005).

[25] J. A. Varnell, C. Edmund, C. E. Schulz, T. T. Fister, R. T. Haasch, J. Timoshenko, A. I. Frenkel, and A. A. Gewirth, Identification of carbon-encapsulated iron nanoparticles as active species in non-precious metal oxygen reduction catalysts, Nat. Commun. **7**, 12582 (2016).

[26] J. Filik *et al.*, Processing two-dimensional x-ray diffraction and small-angle scattering data in DAWN 2, J. Appl. Crystallogr. **50**, 959 (2017).

[27] P. Juhás, T. Davis, C. L. Farrow, and S. J. Billinge, PDFGETX3: A rapid and highly automatable program for processing powder diffraction data into total scattering pair distribution functions, J. Appl. Crystallogr. **46**, 560 (2013).

[28] C. Farrow, P. Juhas, J. Liu, D. Bryndin, E. Božin, J. Bloch, T. Proffen, and S. Billinge, PDFFIT2 and PDFGUI: Computer programs for studying nanostructure in crystals, J. Phys.: Condens. Matter **19**, 335219 (2007).

[29] A. Machida, H. Saitoh, T. Hattori, A. Sano-Furukawa, K.-I. Funakoshi, T. Sato, S.-I. Orimo, and K. Aoki, Hexagonal close-packed iron hydride behind the conventional phase diagram, Sci. Rep. **9**, 12290 (2019).

[30] L. Sandoval-Diaz, M. Plodinec, D. Ivanov, S. Poitel, A. Hammud, H. C. Nerl, R. Schlögl, and T. Lunkenbein, Visualizing the importance of oxide-metal phase transitions in the production of synthesis gas over Ni catalysts, J Energy Chem. **50**, 178 (2020).

[31] A. Cintins, A. Anspoks, J. Purans, A. Kuzmin, J. Timoshenko, P. Vladimirov, T. Gräning, and J. Hoffmann, ODS steel raw material local structure analysis using x-ray absorption spectroscopy, IOP Conf. Ser.: Mater Sci. Eng. **77**, 012029 (2015).

[32] See Supplemental Material at http://link.aps.org/supplemental/10.1103/bqg7-kb24 for Supplemental figures and tables showing EXAFS data fitting results, validation of Eq. (9), and PDF fitting results.

[33] H. Wang *et al.*, Correction of distorted x-ray absorption spectra collected with capillary sample cell, Nucl. Sci. Tech. **34**, 106 (2023).

[34] A. S. Buthelezi, C. L. Tucker, H. J. Heerees, M. L. Shozi, H. H. van de Bovenkamp, and P. Ntola, Fischer-Tropsch synthesis using promoted, unsupported, supported, bimetallic and spray-dried iron catalysts: A review, Results Chem. **9**, 101623 (2024).

[35] M. Lopez Luna, J. Timoshenko, D. Kordus, C. Rettenmaier, S. W. Chee, A. S. Hoffman, S. R. Bare, S. Shaikhutdinov, and B. Roldan Cuenya, Role of the oxide support on the structural and chemical evolution of Fe catalysts during the hydrogenation of CO_2, ACS Catal. **11**, 6175 (2021).

[36] H. Zhou, S. Zhang, Y. Shao, S. Liu, X. Fan, and H. Chen, Relationship between structural properties of the unsupported

Ni_5Ga_3 catalyst and methanol synthesis activity, Ind. Eng. Chem. Res. **63**, 6974 (2024).

[37] M. Onoro, S. Parnell, E. Salas-Colera, D. A. Venero, V. Martin-Diaconesu, T. Leguey, V. de Castro, and M. Auger, Secondary phases characterization by SANS and XAS of an ODS ferritic steel after thermal aging at 873 K, Nucl Mater. Energy **39**, 101671 (2024).

[38] P. A. O'Day, A. Pattammattel, P. Aronstein, V. J. Leppert, and H. J. Forman, Iron speciation in respirable particulate matter and implications for human health, Environ. Sci. Technol. **56**, 7006 (2022).

[39] K. Tirez, G. Silversmit, L. Vincze, K. Servaes, C. Vanhoof, M. Mertens, N. Bleux, and P. Berghmans, Speciation and fractionation of nickel in airborne particulate matter: Comparison between selective leaching and XAS spectroscopy, J. Anal. At. Spectrom. **26**, 517 (2011).

[40] H. Shao, H. Isobe, G. Kitahara, H. Fukui, and A. Yoshiasa, XAFS and XRD study on Fe, Ni, and Ge in iron meteorite NWA 859, Phys. Chem. Miner. **48**, 11 (2021).

[41] S. Boccato *et al.*, Melting properties by x-ray absorption spectroscopy: Common signatures in binary Fe–C, Fe–O, Fe–S and Fe–Si systems, Sci. Rep. **10**, 11663 (2020).

[42] L. Braun *et al.*, Following the structural changes of iron oxides during reduction under transient conditions, ChemSusChem **17**, e202401045 (2024).

[43] N. S. Genz *et al.*, *Operando* laboratory-based multi-edge x-ray absorption near-edge spectroscopy of solid catalysts, Angew. Chem., Int. Ed. **61**, e202209334 (2022).

[44] N. S. Genz, A. J. Kallio, F. Meirer, S. Huotari, and B. M. Weckhuysen, *Operando* laboratory-based x-ray absorption spectroscopy: Guidelines for newcomers in the field, Chemistry-Methods **4**, e202300027 (2024).

[45] M. Rüscher, J. B. Jang, A. Martini, P. Bischoff, W. Frandsen, J. Timoshenko, and B. Roldan Cuenya, Laboratory-based time-resolved *in situ* x-ray absorption spectroscopy for tracking transformations of working electrocatalysts, Chemistry-Methods **4**, 2500016 (2025).